Rapid Growth of Crystalline Mn_5O_8 by Self-Limited Multilayer Deposition using $Mn(EtCp)_2$ and O_3

Matthias J. Young,*,[†,∥] Christopher D. Hare,[‡] Andrew S. Cavanagh,[‡] Charles B. Musgrave,[†,‡] and Steven M. George[‡,§]

[†]Department of Chemical and Biological Engineering, University of Colorado, Boulder, Colorado 80309, United States
[‡]Department of Chemistry and Biochemistry, University of Colorado, Boulder, Colorado 80309, United States
[§]Department of Mechanical Engineering, University of Colorado, Boulder, Colorado 80309, United States

ABSTRACT: This work investigates the use of ozone as a post-treatment of ALD-grown MnO and as a coreactant with bis-(ethylcyclopentadienyl)manganese $(Mn(EtCp)_2)$ in ALD-like film growth. In situ quartz crystal microbalance measurements are used to monitor the mass changes during growth, which are coupled with ex situ materials characterization following deposition to evaluate the resulting film composition and structure. We determined that during O_3 post-treatment of ALD-grown MnO, O_3 oxidizes the near-surface region corresponding to a conversion of 22 Å of the MnO film to MnO_2. Following oxidation by O_3, exposure of $Mn(EtCp)_2$ results in mass gains of over 300 ng/cm^2, which exceeds the expected mass gain for reaction of the $Mn(EtCp)_2$ precursor with surface hydroxyls by over four times. We attribute this high mass gain to adsorbed $Mn(EtCp)_2$ shedding its EtCp ligands at the surface and releasing Mn(II) ions which subsequently diffuse into the bulk film and partially reduce the oxidized film back to MnO. These $Mn(EtCp)_2$ and O_3 reactions are combined in sequential steps with (a) $Mn(EtCp)_2$ reacting at the surface of an O-rich layer, shedding its two EtCp ligands and freeing Mn(II) to diffuse into the film followed by (b) O_3 oxidizing the film surface and withdrawing Mn from the subsurface to create an O-rich layer. This deposition process results in self-limiting multilayer deposition of crystalline Mn_5O_8 films with a density of 4.7 g/cm^3 and an anomalously high growth rate of 5.7 Å/cycle. Mn_5O_8 is a metastable phase of manganese oxide which possesses an intermediate composition between the alternating MnO and MnO_2 compositions of the near-surface during the $Mn(EtCp)_2$ and O_3 exposures.

KEYWORDS: atomic layer deposition, thin film, diffusion-controlled growth, chemical vapor deposition, metastable materials
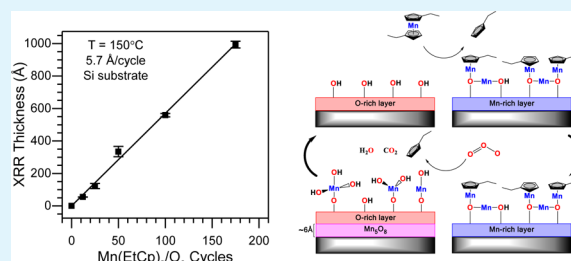
1. INTRODUCTION

Manganese oxides are known to exist with manganese in a single oxidation state, such as MnO (Mn(II)), Mn_2O_3 (Mn(III)), and MnO_2 (Mn(IV)), or in two oxidation states, such as Mn_3O_4 (1Mn(II)/2Mn(III)), Mn_5O_8 (2Mn(II)/3Mn(IV)), and Mn_7O_{12} (4Mn(III)/3Mn(IV)). Most of these stoichiometries also have multiple stable crystal structures, most notably Mn_2O_3[1] and MnO_2.[2] Multiple studies have shown equilibrium transitions to increasingly reduced phases from β-$MnO_2 \rightarrow \alpha$-$Mn_2O_3 \rightarrow Mn_3O_4 \rightarrow$ MnO with increasing temperature, and decreasing O_2 partial pressure.[3,4] The remaining known stoichiometries and crystal structures are metastable and are only observed to exist in controlled environments (e.g., Mn_5O_8),[5,6] or when doped with other cations that stabilize their structures (e.g., Mn_7O_{12}).[7] These various forms of manganese oxide span a wide range of application space encompassing catalysis,[8–10] charge storage,[11,12] and magnetoresistance,[13] among others. Many of these applications exploit the multiple stable valence and spin states of manganese,[14] as well as the diverse electronic structures of its oxides[15,16] arising from various possible stoichiometries and crystal structures.

Thin films of manganese oxide are of particular interest for maximizing the specific surface area of heterogeneous catalysts and high-rate electrochemical charge storage electrodes. To this end, deposition of thin films of manganese oxide has been explored using a variety of approaches including electrochemical techniques,[17,18] pulsed laser deposition (PLD),[19] chemical vapor deposition (CVD),[20,21] and atomic layer deposition (ALD).[22–24] Among these techniques, ALD is distinctive in its ability to produce uniform films with precise thickness control on high aspect-ratio or particulate substrates. In principle, ALD involves sequential, self-limiting surface reactions of gas phase precursors to ideally grow thin conformal films one atomic layer at a time.[25] One disadvantage of ALD that necessarily arises from its atomic layer-by-atomic layer deposition mechanism is its relatively slow deposition rate.

ALD growth of MnO using bis(ethylcyclopentadienyl) manganese $(Mn(EtCp)_2)$ and water (H_2O) has been demonstrated.[22] The +2 oxidation state of Mn in the

$Mn(EtCp)_2$ precursor results in deposition of a Mn-rich MnO phase. This ALD chemistry has been used to deposit MnO as an anode material for lithium ion batteries[26] as well as an electrode material for OER and ORR catalysis.[27] However, thin films of higher oxides of manganese are of interest for a variety of applications, including as electrochemical supercapacitor electrodes,[16,28,29] cathode materials for lithium ion batteries,[30] electrochromic materials,[17] and catalysts.[10]

Higher oxides of manganese for supercapacitors ($NaMn_4O_8$)[31] and lithium ion batteries ($LiMn_2O_4$)[32] can be attained by electrochemical treatment of ALD-grown MnO. However, direct growth of higher oxides is preferable in many instances to reduce complexity and cost of fabrication. One study grew higher oxides of manganese using $Mn(thd)_3$ (Hthd = 2,2,6,6-tetramethylheptan-3,5-dione) and ozone (O_3).[23] The higher +3 oxidation state of Mn in the $Mn(thd)_3$ precursor coupled with O_3 as an oxygen source drives the formation of the higher oxides MnO_2 or Mn_3O_4, depending on the deposition temperature.[23] Another study used ternary chemistries involving either a $Mn(EtCp)_2$ or $Mn(thd)_3$ manganese precursor, a lithium tert-butoxide (LiO^tBu) or Li(thd) lithium precursor, and H_2O or O_3 as the oxygen source to demonstrate that Mn(III)-containing $LiMn_2O_4$ could be grown using $Mn(thd)_3$, (LiO^tBu), and O_3.[33] This study also reported that the use of O_3 with $Mn(EtCp)_2$ resulted in undesirable oxidation of Mn(II), and suggested that treatment with lithium precursors led to subsurface incorporation of lithium.[33]

Ozone has been used as a coreactant with metal precursors in numerous other ALD chemistries, often in an effort to produce a higher oxide of a metal because O_3 is a stronger oxidant than H_2O or O_2.[34,35] In addition to the use of O_3 as an oxygen source coreactant with $Mn(thd)_3$ mentioned above, other studies have used O_3 to yield higher oxides of iridium, (IrO_2),[36] indium, (In_2O_3),[37] cobalt ($LaCoO_3$),[38] rhodium (Rh_2O_3),[39] and platinum (PtO_x).[40] O_3 has also been used as a coreactant with organometallic precursors to reduce carbon contamination. For instance, O_3 was used as a coreactant with ferrocene to deposit Fe_2O_3,[41,42] and with many other carbon containing metal precursors[34] where O_3 oxidizes C on the surface to produce CO or CO_2.

In this work, we present the results of a study of the use of O_3 coupled with the $Mn(EtCp)_2$ precursor to produce higher oxides of manganese. We investigate the use of O_3 as both an oxidizing post-treatment to MnO ALD films grown using $Mn(EtCp)_2$ and H_2O, and as the oxygen source coreactant with $Mn(EtCp)_2$. This work reports a new mechanism for relatively rapid self-limited deposition of conformal, uniform thin films using conventional ALD procedures and reveals the unexpected growth of the Mn_5O_8 metastable polymorph of manganese oxide.

2. MATERIALS AND METHODS

2.1. Sample Preparation. ALD was carried out on ~1″ × 1″ silicon substrates with a native oxide (Si) cut from 6″ silicon wafers (Silicon Valley Microelectronics). Si samples were cleaned with acetone (Fisher, Certified ACS), and methanol (EMD Millipore HPLC grade), dried using ultra high purity nitrogen (Airgas), and loaded into the ALD reactor.

2.2. Growth Conditions. In this work, all reactions were performed in a custom hot-walled ALD reactor at 150−180 °C and ~1 Torr of argon pressure provided by a 120 sccm continuous argon purge (Airgas, Prepurified). ALD of MnO was carried out using (a) $Mn(EtCp)_2$ (>98% Strem Chemicals) and (b) H_2O (B&J Brand HPLC grade), as described previously.[22] A schematic of the ALD

growth process of MnO with these precursors based on this previous work is illustrated in Figure 1. $Mn(EtCp)_2$ was held at 95−100 °C and
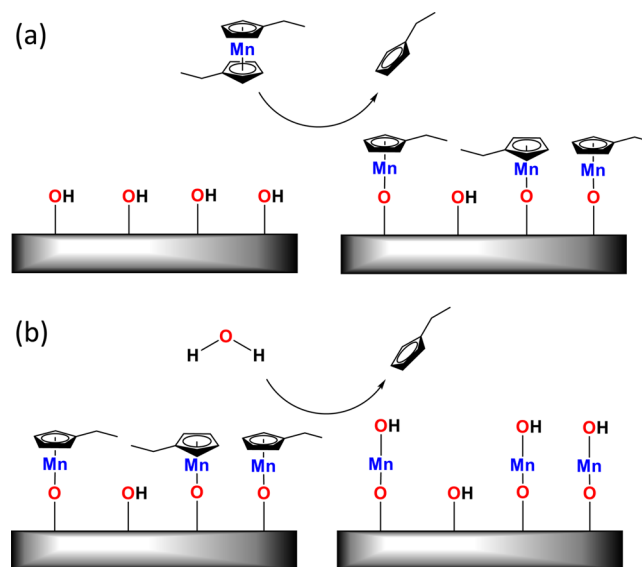

Figure 1. Schematic mechanism of ALD of MnO by sequential exposures of (a) $Mn(EtCp)_2$ and (b) H_2O.

dosed using a flow-over configuration, in which argon was diverted over the headspace of the $Mn(EtCp)_2$ during dosing. The peak pressure of the H_2O dose was tuned to a level ~200 mTorr above the base pressure. The ALD half-reactions using the $Mn(EtCp)_2/H_2O$ chemistry to deposit MnO were performed in an $Mn(EtCp)_2$/Purge/H_2O/Purge sequence, with a typical timing of 0.5s/45s/0.2s/45s.

2.3. Ozone Exposure. In this work, O_3 is studied both as an oxidizing post-treatment where ALD-grown MnO is exposed to O_3 and as a coreactant with $Mn(EtCp)_2$. O_3 is generated from a 95% O_2:5% N_2 supply (Airgas) using a 0.7 kW ozone generator (CFS-1, Ozonia) with the generator power and flow rate tuned to produce a continuous effluent stream of ~10% O_3. A fraction of this ozone-containing stream is diverted into the reactor during O_3 doses. These doses are reported below as total pressures above base-pressure. The range of 0.5−8 Torr dose pressures we report correspond to O_3 partial pressures of ~0.05−0.8 Torr, with the remaining pressure composed of O_2 and N_2. O_3 dose times are 60 s unless indicated otherwise. The O_3 dosing line is heated to the temperature of the reactor. The fraction of the O_3-containing stream which does not flow into the reactor is sent to an ozone destruct (HA-212, Ozone Engineering) and the resulting products exhausted. We note that no growth was observed when O_2 was used in place of O_3.

2.4. Quartz Crystal Microbalance. Quartz Crystal Microbalance (QCM) measurements were taken using AT-cut quartz crystals (Colorado Crystal Corporation) in conjunction with a Q-Pod quartz crystal monitor and data collection software (Inficon). These measurements were performed during reactions using a free-floating QCM crystal. This configuration was preferred for this work due to pressure swings of ~10 Torr during O_3 doses, making use of the standard one-sided QCM measurements[43] difficult. In a free-floating crystal configuration, growth takes place on both sides of the QCM crystal. Therefore, we expected the measured mass gain to be approximately twice that of growth on one side of the QCM crystal. Indeed, for the MnO ALD chemistry, dividing the measured mass gain per cycle (MGPC) by a factor of 2 produced a calculated MGPC of 60 ng/cm^2/cycle, which agrees with the previously reported value of 56 ng/cm^2/cycle for $Mn(EtCp)_2/H_2O$.[22] Mass changes reported below have been divided by a factor of 2 to represent growth per square centimeter of QCM surface area.

2.5. X-ray Characterization. The thickness, density, and roughness of films deposited on Si wafers were evaluated ex situ

using X-ray Reflectivity (XRR), while film crystallinity was evaluated using Glancing Incidence X-ray Diffraction (GIXRD). XRR and GIXRD measurements were performed using a Bede D-1 X-ray Diffractometer (Jordan Valley Semiconductors). X-ray radiation with a wavelength of 1.54 Å was used for these measurements, corresponding to the Cu−Kα transition from the X-ray filament. Film thickness, density, and roughness were modeled using the Bede REFS software package (Jordan Valley Semiconductors). For GIXRD measurements, the glancing incidence angle, ω, was set to 0.5°, just above the critical angle measured for manganese oxide films by XRR. The step size was ≤0.05 arcseconds for every GIXRD measurement, and the count time was ≥20 s. Measured GIXRD spectra were compared with simulated powder XRD spectra of crystal structures from the experimental Inorganic Crystal Structure Database (ICSD)[44] using the RIETAN-FP•VENUS[45] package.

2.6. X-ray Photoelectron Spectroscopy. After growth, ~0.25″ × 0.25″ squares were cut from silicon wafers and loaded into an XPS analysis chamber. A PHI 5600 X-ray photoelectron spectrometer (RBD Instruments) was employed with monochromatic Al Kα X-rays at an energy of 1486.6 eV. An argon ion beam was rastered over the sample for 2 min to remove adventitious carbon before XPS measurement. XPS spectra were acquired using a pass energy of 58.7 eV and a step size of 0.25 eV. An electron beam neutralizer was employed at 17.8 mA. Data were obtained with the Auger Scan control program (RBD Instruments) and analyzed using CASA XPS software (Casa Software).

2.7. Rutherford Backscattering Spectrometry. Rutherford Backscattering Spectrometry (RBS) measurements were performed at the University of Minnesota Characterization Facility using a MAS 1700 pelletron tandem ion accelerator (5SDH) equipped with charge exchange RF plasma source by National Electrostatics Corporation (NEC). The incident beam was 2 MeV He$^+$, oriented normal to the sample surface, and backscattered ions were detected at a 165° scattering angle. An analytical endstation (RBS 400) and NEC control software were used for spectral data acquisition across 2048 data channels calibrated to 3.02 keV per channel, with a total energy resolution of ~18 keV. The raw spectra were simulated using QUARK freeware software to yield elemental composition and elemental areal density in the films.

3. RESULTS AND DISCUSSION

3.1. Post-treatment of MnO with O$_3$ and Mn(EtCp)$_2$.
3.1.1. Oxidation of ALD-MnO by O$_3$ Exposure. In situ QCM experiments were used to determine the extent to which O$_3$ exposure oxidizes an ALD-grown MnO film. ALD deposition of 100 cycles of trimethylaluminum and water (~10 nm Al$_2$O$_3$) was used to cap the QCM crystal surface before each experiment. Varying thicknesses of MnO were subsequently deposited onto the QCM crystal using the Mn(EtCp)$_2$/H$_2$O ALD chemistry. Following the MnO growth, ~2 Torr of O$_3$ was dosed into the chamber for 2 min during which the mass change on the QCM crystal was monitored. A QCM trace showing MnO growth with subsequent O$_3$ exposure is shown in Figure 2. In this trace, the growth of MnO proceeds with 1.2 μg/cm^2 of mass gain after 20 ALD cycles corresponding to a MGPC of 60 ng/cm^2/cycle. This value closely agrees with the expected value of 56 ng/cm^2/cycle.[22] During the subsequent O$_3$ dose the QCM mass signal increases and then briefly drops. We attribute this drop in signal to local heating of the QCM crystal by the exothermic decomposition of O$_3$ at the crystal surface.[46] When the O$_3$ dose stops, the exothermic decomposition of O$_3$ ceases, the crystal cools to the temperature of the reaction chamber, and the mass signal increases above the level measured prior to the O$_3$ exposure.

The final mass gain due to the O$_3$ pulse is attributed to an uptake of oxygen into the MnO film. The total mass gain resulting from the O$_3$ exposure shown by the QCM plot in
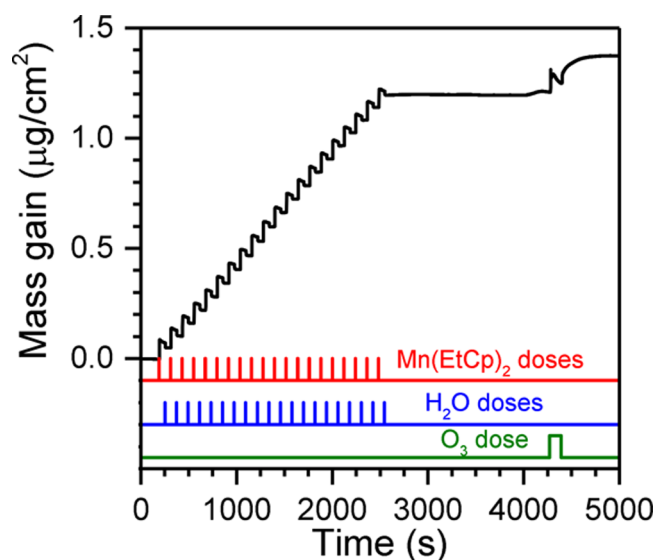

Figure 2. QCM trace of 20 MnO ALD cycles followed by an O$_3$ exposure of 2 Torr for 2 min at 150 °C.

Figure 2 is 1.37 μg/cm^2. This is in stark contrast to the mass *loss* of 0.0265 μg/cm^2 observed from H$_2$O exposure for the Mn(EtCp)$_2$/H$_2$O ALD chemistry[22] as depicted in Figure 1b, and corresponds to a 14% increase in the mass of the manganese oxide film. Prior work indicates that at this temperature and oxygen partial pressure, MnO favorably converts to MnO$_2$.[3,4] Furthermore, O$_3$ has been demonstrated to produce highly oxidized manganese peroxide surface species, which could result in an additional mass gain.[46] However, if the entire MnO film were converted to MnO$_2$, then the mass gain would be 23.6%. This indicates that only a fraction of the MnO thin film is oxidized by O$_3$ exposure.

We propose that oxidation of the MnO film by O$_3$ exposure extends into the bulk film through Mn diffusion from the underlying MnO to the surface. As O$_3$ reacts at the surface, highly oxidized species (e.g., MnO$_2$[3,4] and Mn-peroxides[46]) are formed, and Mn(II) ions diffuse from the bulk to the surface where they reduce these oxidized species and create Mn vacancies in the underlying MnO film. A composite analysis of defect migration in MnO at elevated temperatures (>1000 °C) produces a value for the activation energy of bulk Mn vacancy diffusion in MnO of 51.8 kcal/mol.[47] At temperatures of 150−180 °C for the work presented here, the 51.8 kcal/mol activation energy limits Mn vacancy migration in MnO. While O diffusion may also contribute to the bulk oxidation, we could find no reported values (e.g., barrier or diffusivity) to estimate the rate of oxygen diffusion in manganese oxides. However, in general, less polarizable ions are expected to have a higher rate of diffusion in a given material as vacancies of the less polarizable ion are more readily stabilized by the surrounding structure.[48] Electronic polarizabilities of 1.99 Å^3 for O^{2-} and 1.39 Å^3 for Mn^{2+} were determined from refractive index data.[49] On the basis of these data, we expect O diffusion to be slower than Mn diffusion in MnO, which is slow based on the 51.8 kcal/mol activation energy for Mn diffusion. Thus, slow Mn and O diffusion limit the depth to which MnO oxidizes upon exposure to O$_3$ and explains the incomplete oxidation we observe. In Figure 3, the mass gain from O$_3$ exposure is plotted against the initial mass of MnO deposited for an array of QCM experiments. In this figure, the diagonal dashed line has a slope
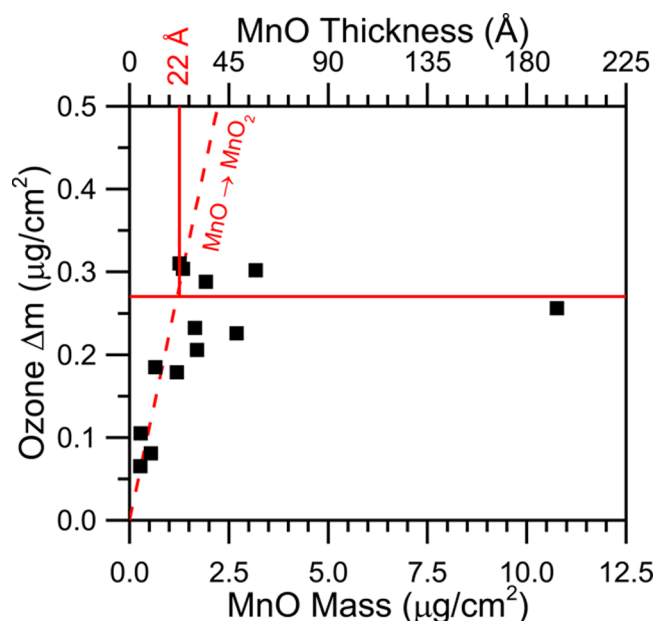
Figure 3. Mass change from O_3 exposure versus the mass of MnO deposited. A secondary *x*-axis shows the initial MnO thickness as calculated from average MnO growth rates and densities. The diagonal dashed line represents the predicted mass change for MnO conversion to MnO_2.

Figure 4. QCM trace of O_3 pulse and 15 successive 0.5 s $Mn(EtCp)_2$ pulses onto MnO film grown with 25 ALD cycles.

of 0.236, corresponding to the fractional mass gain expected for complete conversion of MnO to MnO_2 and neglecting any formation of peroxide surface species. Figure 3 shows that for MnO thicknesses of up to 22 Å, the observed mass gains for most samples correspond to the expected mass gains for complete conversion of MnO to MnO_2. However, for thicknesses ≥22 Å, the mass gain is limited to a roughly constant value. This indicates that the surface of thicker MnO films oxidizes up to a depth of only 22 Å and supports our hypothesis that slow bulk diffusion of Mn and O limits the depth to which MnO converts to MnO_2 under ozone exposure. The 200 Å MnO thickness condition in Figure 3 confirms that the oxidation behavior we observe is not limited to the nucleation regime of the MnO chemistry.

3.1.2. Saturation of $Mn(EtCp)_2$ Following O_3 Exposure. In order to determine whether a saturating dose of $Mn(EtCp)_2$ can be achieved following an O_3 exposure, 15 successive 0.5 s pulses of $Mn(EtCp)_2$ were performed following each O_3 exposure (described in the previous section). Figure 4 shows a QCM trace of a typical O_3 exposure with successive $Mn(EtCp)_2$ pulses. For these experiments, the reactor was purged for at least 10 min following the O_3 exposure prior to the $Mn(EtCp)_2$ doses. No mass loss was observed during this purge time, indicating that the film oxidation by O_3 does not spontaneously reverse. It is evident in Figure 4 that a saturating dose of $Mn(EtCp)_2$ can be achieved on O_3-treated MnO surfaces as is desirable for ALD growth.[25,50] However, this saturation requires a large exposure of $Mn(EtCp)_2$. After the first 0.5 s $Mn(EtCp)_2$ pulse, only 70% of the final mass gain is realized. Furthermore, the mass gain following these 15 $Mn(EtCp)_2$ pulses is substantially higher than expected for the reaction of the $Mn(EtCp)_2$ precursor with surface hydroxyls as depicted in Figure 1a.

Remarkably, the mass gain following 15 $Mn(EtCp)_2$ pulses of 342 ng/cm² (shown in Figure 4) is over four times the mass gain of ~80 ng/cm² observed for the surface reaction of
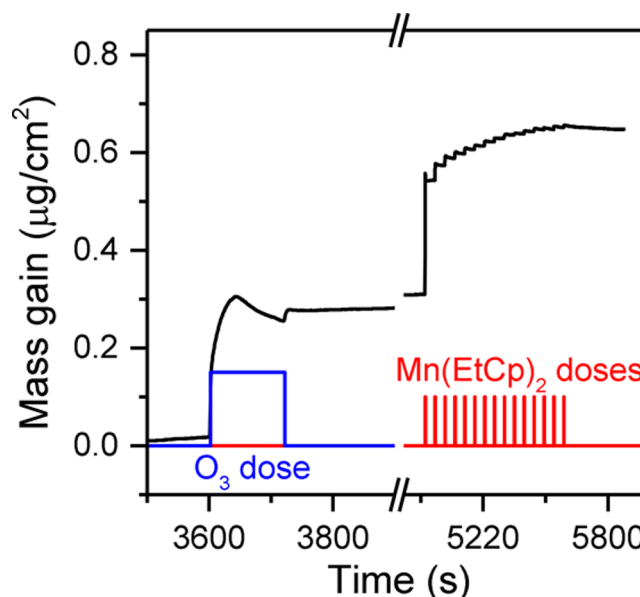
$Mn(EtCp)_2$ during the deposition of $Mn(EtCp)_2$/H_2O ALD chemistry,[22] and approximately three times the mass gain of 116 ng/cm² expected for a monolayer of MnO based on the ICSD structure.[44] This result suggests that a considerable amount of Mn readily incorporates into the oxidized film that results from O_3 exposure. Indeed, if any residual peroxide surface species are present, the hydroxides they provide would enable additional $Mn(EtCp)_2$ to react.

We also propose that rapid Mn and O diffusion in the oxidized film enables Mn to penetrate into the subsurface of the film. Mn diffusion has an activation barrier of 34 kcal/mol in pristine MnO_2 and is mediated by Mn vacancies.[51] However, in the presence of 6% Mn vacancies this barrier decreases to 19 kcal/mol.[51] These activation energies are significantly lower than the 51.8 kcal/mol barrier reported for Mn diffusion in MnO,[47] and indicate that Mn diffusion in MnO_2 is thermally accessible at the 150 °C growth temperature used in this work. In higher oxides of manganese, we expect the rate of O diffusion to play a greater role in film conversion, arising from the larger polarizability of Mn ions with higher formal charges.[49] In addition to Mn ions diffusing into the bulk film, O ions will also diffuse from the bulk film toward the film surface. We also expect that the rate of Mn and O diffusion will slow as more Mn is incorporated into the film. As Mn ions diffuse into the oxidized (MnO_2) film, we expect them to fill Mn vacancies, thereby slowing Mn diffusion. Additionally, conversion of the film surface to MnO by $Mn(EtCp)_2$ will also create a barrier to Mn and O diffusion, preventing the conversion to MnO from extending into the bulk film. The mechanism we describe here for the migration of Mn from the surface into the bulk film accounts for the large $Mn(EtCp)_2$ exposure needed to achieve saturation.

The mass gain following 15 $Mn(EtCp)_2$ pulses for an O_3-treated surface versus the initial MnO thickness is shown in Figure 5. Unfortunately, large uncertainties for the thinnest MnO thicknesses in Figure 5 preclude an analysis of the extent of $Mn(EtCp)_2$ reaction versus initial MnO thickness. However, the mass gain following $Mn(EtCp)_2$ exposure does not dramatically increase for larger MnO thicknesses. For all
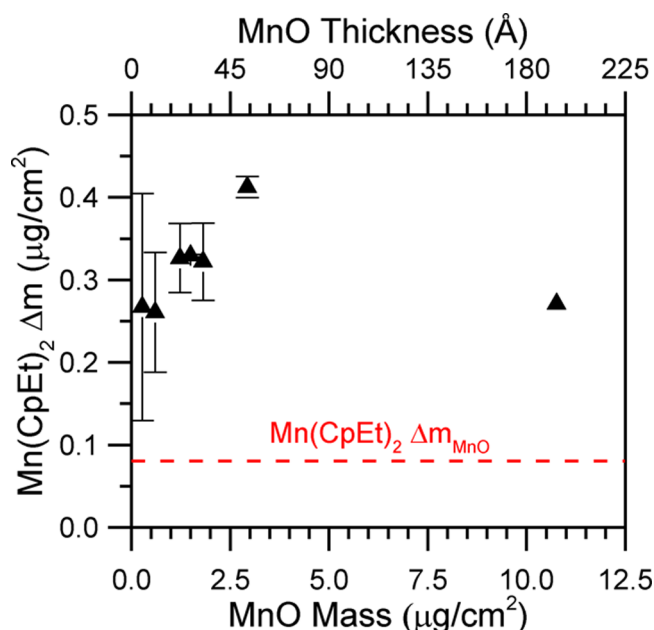
Figure 5. Mass change following 15 $Mn(EtCp)_2$ pulses subsequent to O_3 exposure versus the initial mass of MnO. A secondary x-axis shows the initial MnO thickness as calculated from average MnO growth rates and densities. The horizontal dashed line indicates the expected mass change for reaction of $Mn(EtCp)_2$ with surface hydroxyls.

MnO thicknesses, the mass gain following exposure to $Mn(EtCp)_2$ is three to five times higher than the mass gain measured for a saturating dose of $Mn(EtCp)_2$ during ALD using the $Mn(EtCp)_2/H_2O$ chemistry.[22] This result supports a mechanism in which Mn supplied by the surface reactions of the $Mn(EtCp)_2$ precursor not only reacts with the surface of the manganese oxide film, but Mn(II) likely diffuses into the oxidized film and reduces subsurface Mn(III) or Mn(IV) centers. We expect that this unique subsurface reactivity will extend the possible growth rates and stoichiometries achievable with depositions by ALD-like growth processes. For instance, in order to grow higher oxides of manganese, the $Mn(EtCp)_2$ exposure should be restricted to limit the diffusion of Mn^{2+} into the bulk film. We suggest that other metal oxides with stable phases of different metal oxidation states may exhibit similar behavior when the oxidant and/or metal precursor exposure switches the equilibrium stable phase between metal oxides with different stoichiometries.

3.2. Film growth by sequential exposures of Mn-(EtCp)$_2$ and O$_3$. *3.2.1. Saturation of O$_3$ During Manganese Oxide Growth Using Mn(EtCp)$_2$/O$_3$.* In order to study the saturation behavior of O_3 during $Mn(EtCp)_2/O_3$ growth, 50 cycles of $Mn(EtCp)_2/O_3$ were deposited on silicon wafers using varying O_3 exposures, and the resulting thin films were analyzed using XRR. For the growth of these films, purge times of 45 s were used following each dose, and $Mn(EtCp)_2$ was pulsed for 0.5 s. For Figure 6, we limited the $Mn(EtCp)_2$ exposure to a practical amount for efficient steady-state growth and determined the necessary O_3 exposure to achieve saturation. From Figure 4, one 0.5 s $Mn(EtCp)_2$ dose yields a mass gain of ~70% of the saturated value. Under larger $Mn(EtCp)_2$ exposures the growth rate per cycle is expected to increase. However, the required O_3 dose for saturation and growth time to achieve a desired thickness would increase considerably.
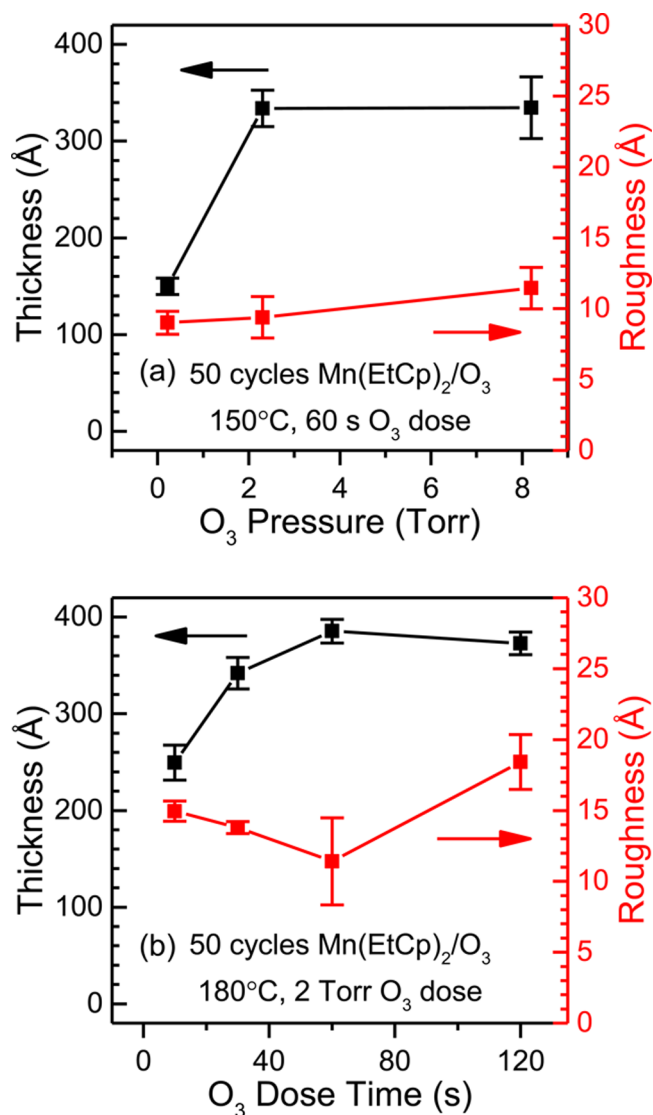

Figure 6. Thickness and density of films resulting from 50 cycles of $Mn(EtCp)_2$ and O_3 versus (a) O_3 dose pressure and (b) O_3 dose time.

Figure 6a,b shows modeled XRR thicknesses and roughnesses versus O_3 partial pressure and pulse time, respectively. No difference in growth rate between 2 and 8 Torr O_3 dose pressures is observed (Figure 6a) suggesting that saturation has been reached during a 2 Torr dose of O_3 for 60 s. We note that the film thickness for the case of 50 cycles at 8 Torr O_3 dose pressure in Figure 6a corresponds to a growth rate of 6.7 ± 0.6 Å/cycle, which is higher than the steady-state growth rate of 5.7 Å/cycle we report below. The slight increase in roughness at 8 Torr may indicate that some surface etching occurs at this higher O_3 exposure. While the MnO_3OH surface species reported in prior work[46] is a likely leaving group for surface etching, further experiments are necessary to identify any Mn-containing volatile products upon ozone exposure.

Figure 6b shows that for a 2 Torr O_3 exposure, a dose time longer than 30 s is required to reach saturation. Again, the slight increase in roughness and decrease in thickness for 120 s of dose time at this O_3 pressure indicate that etching of the film at higher O_3 exposures may have occurred. We attribute the higher growth rate in Figure 6b to the higher temperature of 180 °C used in this experiment, which enables faster Mn and O

diffusion and a greater extent of reaction. The results in Figure 6 indicate that an O_3 exposure of at least 2 Torr for 30 s is necessary for saturation following one 0.5 s $Mn(EtCp)_2$ dose. The necessity for such a large O_3 exposure to achieve saturation is expected considering the known recombination of O_3 during ALD processes[35] and decomposition of ozone on manganese oxide surfaces.[46] The effect of O_3 exposure on the film structure and composition is discussed further below.

3.2.2. In Situ Measurement of Steady-State Mn(EtCp)$_2$/O$_3$ Growth. In situ QCM traces of steady-state growth of $Mn(EtCp)_2$ and O_3 measured during 40 cycles after nucleation is shown in Figure 7. Here, O_3 was dosed at 2 Torr for 60 s,
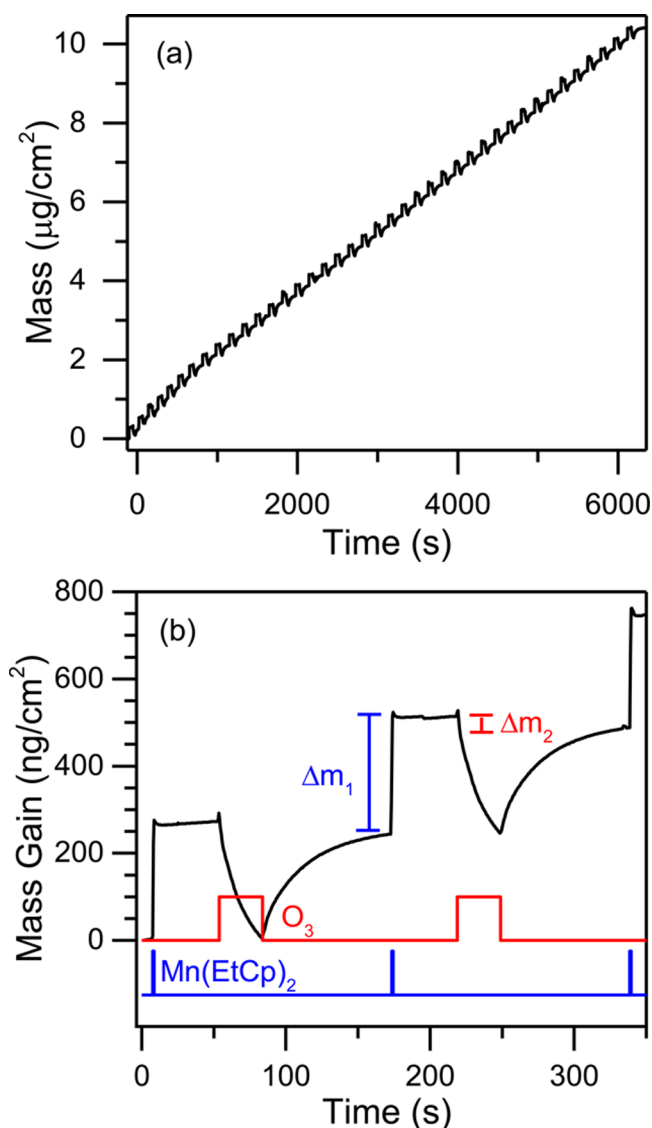

Figure 7. QCM trace of (a) 40 cycles of $Mn(EtCp)_2$ and O_3, and (b) zoomed-in view of cycles 17−19, at $Mn(EtCp)_2$ dose time of 0.5 s and O_3 exposure of 2 Torr for 60 s.

while $Mn(EtCp)_2$ was dosed for only 0.5 s, intentionally undersaturating the $Mn(EtCp)_2$ exposure to enable more rapid saturation during the O_3 exposure. The measured growth is linear over the 40 cycles shown in Figure 7a. However, for these 40 cycles we measure a total mass gain of ~10.4 $\mu g/cm^2$. This corresponds to a remarkable MGPC of ~260 ng/cm^2/cycle, which is ~4 times the mass gain per cycle observed for MnO.[22]

Here, sequential, self-limiting exposures of gas-phase coreactants ($Mn(EtCp)_2$ and O_3) to a material surface results in thin-film growth markedly similar to ALD except for the substantially higher deposition rates. However, the large mass gains we observe each cycle arise from subsurface reactivity, meaning that the film does not grow atomic layer-by-atomic layer, rather, each cycle results in multiple atomic layers. As supported by the analysis presented above, the steady-state growth we observe proceeds by a new mechanism, which we term self-limited multilayer deposition (SLMD).

The mass changes from the $Mn(EtCp)_2$ exposure, Δm_1, and the O_3 exposure, Δm_2, for cycles 17−19 of this deposition are depicted in Figure 7b. Over the 40 SLMD cycles shown in Figure 7a, the average mass changes are $\Delta m_1 = 280 \pm 7$ ng/cm^2 and $\Delta m_2 = -23 \pm 5$ ng/cm^2, with an overall mass gain per cycle of 259 ± 8 ng/cm^2/cycle. The large mass gain during the $Mn(EtCp)_2$ dose agrees with the measurements discussed above and suggests that Mn also incorporates into the subsurface of the film during steady-state growth.

The mass loss we observe from O_3 exposure is surprising considering the large mass gain measured for O_3 exposure to MnO as discussed above. The mass loss observed here from the O_3 exposure during steady-state growth of $Mn(EtCp)_2$/O_3 is comparable in magnitude to the mass loss measured during the H_2O exposure of the $Mn(EtCp)_2$/H_2O chemistry[22] as depicted in Figure 1b. However, the mass gain from $Mn(EtCp)_2$ doses during $Mn(EtCp)_2$/O_3 growth is consistently higher than would be expected for a surface reaction of O_3, indicating that different processes must occur during the O_3 exposure. This result suggests that O_3 exposure during steady-state growth of $Mn(EtCp)_2$/O_3 characteristically differs from the exposure of O_3 to a pristine MnO film. We attribute the mass loss from the O_3 exposure during steady-state growth to the removal of residual carbon and EtCp ligands left by $Mn(EtCp)_2$, which offset the mass gain from oxygen uptake. Film etching from O_3, as discussed above, may also contribute to this observed mass loss. Unfortunately, the multilayer deposition and subsurface penetration of Mn is nonstoichiometric, which complicates a deep mechanistic analysis of these mass changes to further evaluate this mechanism.

3.2.3. Ex Situ Analysis of Films Deposited by Mn(EtCp)$_2$/O$_3$. Ex situ XRR thickness measurements after varying numbers of cycles of $Mn(EtCp)_2$/O_3 deposition using a 0.5 s dose of $Mn(EtCp)_2$ and an O_3 dose of 8 Torr for 60 s are presented in Figure 8. This figure shows that the film thickness increases linearly with the number of cycles up to 175 cycles. Using a linear fit, the growth rate from these measurements is found to be 5.7 Å/cycle. By evaluating the standard deviation of each thickness in Figure 8, the mean absolute error in the growth rate is calculated to be ±0.3 Å/cycle. This growth rate is significantly higher than the growth rates of 0.2 Å/cycle observed for MnO_2 deposition by ALD,[23,33] and ~1 Å/cycle for MnO deposition by ALD[22] and supports the assertion that the growth of $Mn(EtCp)_2$/O_3 occurs as SLMD. Visually, films were pristine and uniform and despite the high growth rate, modeled XRR roughnesses were ≤20 Å for all film thicknesses, indicating conformal and uniform growth. This higher growth rate with good film quality has practical appeal as it requires fewer deposition cycles than traditional ALD to reach a desired thickness.

The XRR fitting for the set of samples in Figure 8 yields an average density of 4.7 g/cm^3. Using the growth rate and density from XRR yields a MGPC of 268 ng/cm^2/cycle, which is
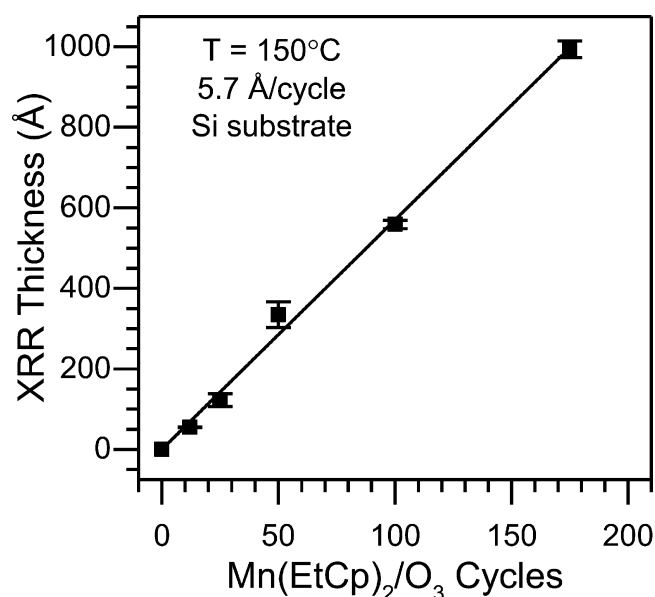
Figure 8. Film thickness from ex situ XRR measurements on Si wafers versus number of $Mn(EtCp)_2/O_3$ cycles with 0.5 s $Mn(EtCp)_2$ dose time and O_3 exposure of 8 Torr for 60 s.

consistent with the value of 259 ± 8 $ng/cm^2/cycle$ from in situ QCM measurements reported above. While the density of 4.7 g/cm^3 is similar to the densities of multiple manganese oxide stoichiometries (MnO: 5.37 g/cm^3, Mn_3O_4: 4.87 g/cm^3, Mn_2O_3: 5 g/cm^3, MnO_2 5.08 g/cm^3),[52] it is closest to the theoretical density of Mn_5O_8 of 4.8 g/cm^3 as computed from the ICSD crystal structure.[44]

GIXRD measurements of films of varying thicknesses grown using varying O_3 dose pressures are presented in Figure 9. A measured spectrum for a bare Si wafer, as well as reference spectra for Mn_5O_8 and Mn_3O_4 are shown for comparison. For O_3 dose pressures of 2 and 8 Torr, multiple peaks are visible with similar peak heights and widths, suggesting that films grown using both of these ozone dose pressures contain similar crystalline domains. The diffraction peaks for a 175 cycle deposition shows more pronounced peaks than the 50 cycle sample (both at 8 Torr) due to the stronger signal generated from the thicker sample. The peak widths are broad for all film thicknesses, suggesting small crystalline domains.[53] Although many of the peaks in our measured spectra agree with Mn_5O_8, the two most prominent peaks we observe at ~32° and ~37° also agree with the reference spectrum for Mn_3O_4. The modeled density from XRR measurements is also close to the value expected for Mn_3O_4, preventing a conclusive interpretation of the GIXRD data at this juncture.

The compositions of the manganese oxide films grown at varying pressures of O_3 as measured by XPS are shown in Figure 10. The composition of the manganese oxide film is dependent on the O_3 dose pressure used. For 200 mTorr of O_3 dose pressure, the resulting film contains over 10% carbon, and has an O:Mn stoichiometric ratio of 1:1. This indicates that at this exposure O_3 only partially oxidizes the manganese oxide film and removes a fraction of the carbon deposited from the surface EtCp ligands. In contrast, for both 2 and 8 Torr O_3 dose pressures, the carbon content is below the detection limit of the XPS, and the O:Mn ratios were measured to be 1.80 and 1.74, respectively. These ratios fall between the values expected for Mn_2O_3 (1.5) and MnO_2 (2.0) and are closer to the value
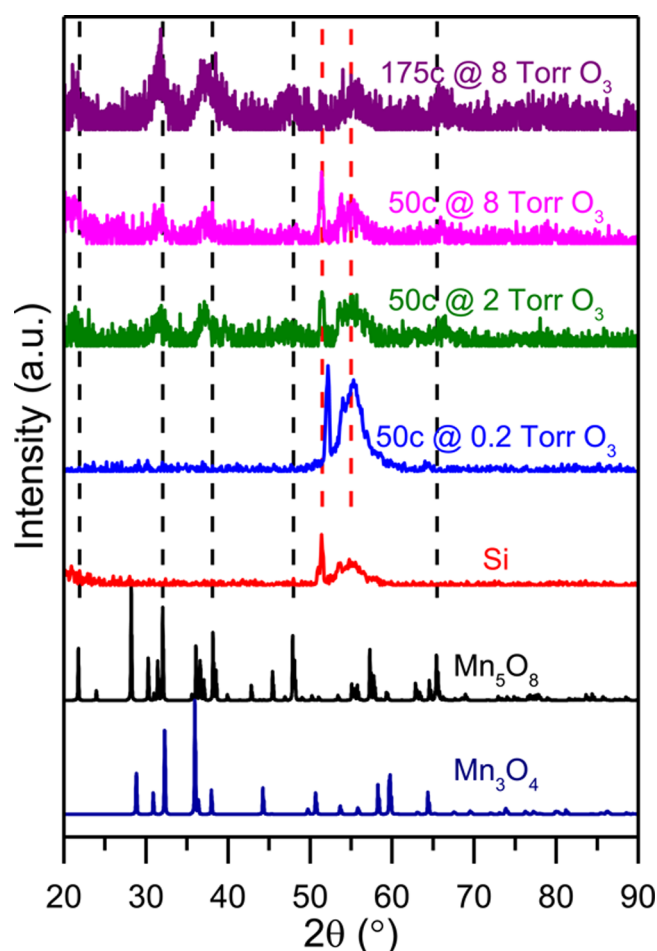

Figure 9. GIXRD measurements on Si wafers following $Mn(EtCp)_2/O_3$ depositions for varying numbers of SLMD cycles and O_3 dose pressures. Bare Si wafer and crystalline Mn_5O_8 and Mn_3O_4 spectra are shown for reference.
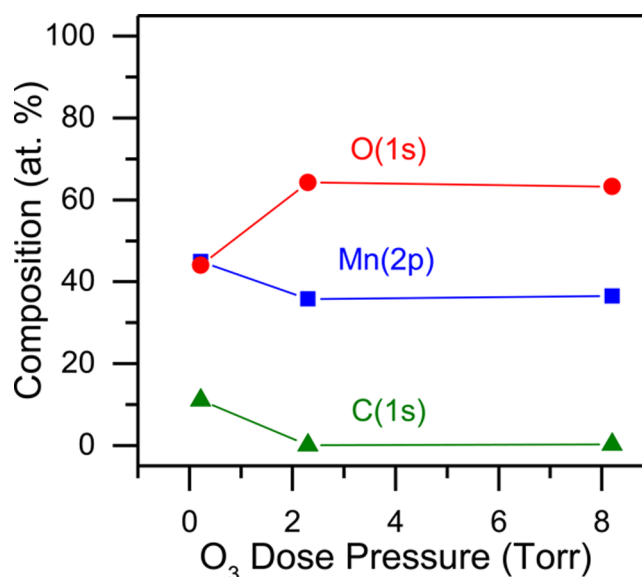

Figure 10. XPS composition after removal of adventitious carbon for films grown by 50 SLMD cycles of $Mn(EtCp)_2$ and O_3 versus O_3 dose pressure.

expected for Mn_5O_8 (1.6) than the value expected for Mn_3O_4 (1.25). This result coupled with the XRR and GIXRD results presented above suggests that the deposited film is Mn_5O_8. However, the surface sensitivity of XPS along with the possibility of preferential sputtering of Mn or O during the removal of adventitious carbon may make the XPS results less conclusive.

In order to resolve the ambiguity of the above results, RBS was performed to determine the composition of these SLMD manganese oxide films. RBS was carried out on a Si sample with 175 SLMD cycles of $Mn(EtCp)_2/O_3$ deposited at 150 °C with a 0.5 s $Mn(EtCp)_2$ dose time and a 60 s O_3 exposure at 8 Torr, as presented in Figure 11. The manganese oxide film thickness

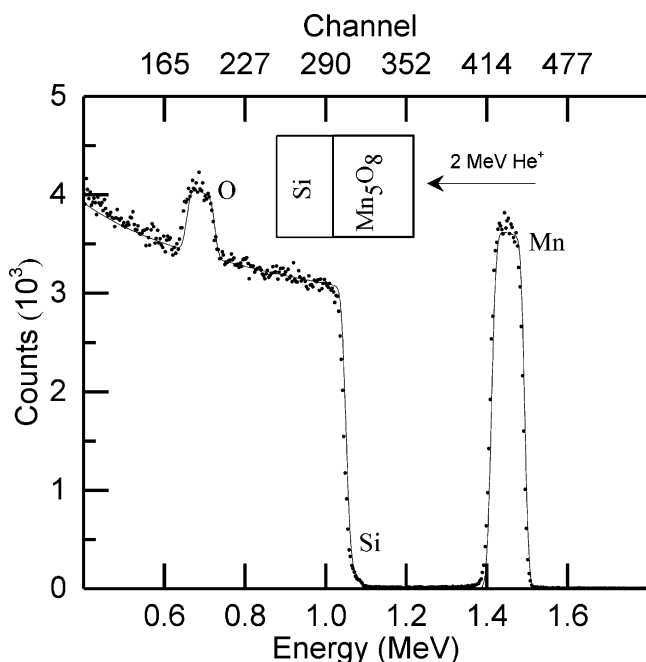**Figure 11.** RBS measurement on Si wafer following 175 SLMD cycles of $Mn(EtCp)_2/O_3$ at 150 °C with 0.5 s $Mn(EtCp)_2$ dose time and O_3 exposure of 8 Torr for 60 s with corresponding fit for Mn_5O_8.

of this sample was 101 nm from XRR. Fitting the RBS spectrum yields a bulk composition of Mn_5O_8. These data, coupled with the GIXRD, XRR, and XPS data presented above, provide strong support that the $Mn(EtCp)_2/O_3$ chemistry results in SLMD growth of crystalline Mn_5O_8.

The formation of Mn_5O_8 using this deposition technique is surprising. Mn_5O_8 is a metastable polymorph of manganese oxide,[5,6] which is not expected to form upon oxidation of MnO.[3,4] However, the repeated oxidation of the film by O_3 to form Mn(IV) and exposure of $Mn(EtCp)_2$ as the source of Mn(II) seemingly provides the necessary conditions for the stable coexistence of these two valence states of manganese in the form of Mn_5O_8. This technique for growing thin-films of Mn_5O_8 is especially exciting considering the recent demonstration of nanoscale Mn_5O_8 as a catalyst for OER.[10]

4. SUMMARY

In this work, we studied the reaction of O_3 as a post-treatment of ALD-grown MnO and as a coreactant with $Mn(EtCp)_2$ during growth. As a post-treatment to ALD-grown MnO, we determined that O_3 oxidizes a near-surface region of ALD-grown MnO corresponding to the conversion of 22 Å of the

MnO film to MnO_2. Following oxidation by O_3, exposures of $Mn(EtCp)_2$ result in mass gains exceeding 300 ng/cm^2. This mass gain is more than four times that expected from ligand exchange surface reactions of the $Mn(EtCp)_2$ precursor with surface hydroxyls. This suggests that $Mn(EtCp)_2$ contributes to a bulk reduction reaction following O_3 exposure, where Mn(II) reduces the surface to MnO and Mn diffuses into the bulk material.

As a coreactant with $Mn(EtCp)_2$, we determined a dependence of the growth rate and composition of the resulting films on the O_3 dose pressure. Saturated growth occurred at O_3 dose pressures >2 Torr and dose times >30 s and yielded carbon-free films with growth rates >5 Å/cycle. In contrast, an O_3 exposure of 200 mTorr for 60 s resulted in an incomplete reaction, yielding growth rates of ~3 Å/cycle and carbon content from XPS measurements exceeding 10%. Additionally, we observe an increase in roughness and decrease in growth rate upon overexposure to O_3.

For a 30 s O_3 dose at 2 Torr, we observed self-limited multilayer deposition of pristine and uniform films of crystalline Mn_5O_8 with a density of 4.7 g/cm^3 and an anomalously high growth rate of 5.7 Å/cycle from XRR. The growth of Mn_5O_8 is verified by ex situ GIXRD, XPS, and RBS. Furthermore, in situ QCM analysis of steady-state growth yielded a mass gain per cycle of 259 ± 8 ng/cm^2/cycle, with a mass gains of $\Delta m_1 = 280 \pm 7$ ng/cm^2 from the $Mn(EtCp)_2$ exposure and a mass loss of $\Delta m_2 = -23 \pm 5$ ng/cm^2 from the O_3 exposure. The large growth rate and mass gain per cycle corroborate the picture that $Mn(EtCp)_2/O_3$ growth deposits more than one atomic layer per cycle.

5. GENERAL CONCLUSIONS

Film deposition by sequential gas-phase doses of $Mn(EtCp)_2$ and O_3 is shown to exhibit unique chemical behavior and rapid film growth. Growth is self-limited, but yields an anomalously high growth rate of ~6 Å/cycle and mass increase of ~300 ng/cm^2/cycle. This deposition rate is ~5−20 times higher than known manganese oxide ALD chemistries and exceeds growth rates accessible by surface ligand exchange reactions. Such a rapid growth rate requires fewer cycles to produce uniform conformal films of a desired thickness, thereby decreasing fabrication time and cost. This efficient chemistry can be used to rapidly deposit thin films of manganese oxide for applications including catalysis, energy storage, and electrochromism.

We suggest that rapid growth for the $Mn(EtCp)_2/O_3$ chemistry is enabled by kinetically accessible bulk Mn and O diffusion in higher oxides of Mn. This allows Mn to diffuse to the surface during O_3 exposures, and to diffuse into the bulk during $Mn(EtCp)_2$ exposures, causing more precursor to react during each half-cycle. We expect analogous behavior to occur during the growth of other metals oxides with stable phases of different metal oxidation states. This behavior will likely occur when a strong oxidant, such as O_3, and/or a metal precursor switch the equilibrium stable phase between metal oxides with different stoichiometries. By taking advantage of this mechanism, rapid growth by SLMD can likely be achieved for other metal oxides.

Growth of $Mn(EtCp)_2/O_3$ under the conditions in this work produces crystalline Mn_5O_8, a metastable phase of manganese oxide which nominally contains both Mn(II) and Mn(IV). We attribute the formation of this phase to the shifting chemical equilibrium during growth. $Mn(EtCp)_2$ shifts the chemical

equilibrium toward Mn(II), while O_3 shifts the chemical equilibrium toward Mn(IV) (or higher Mn oxidation states). Coupling these steps yields an intermediate and metastable bulk composition. The controlled growth of metastable materials has attracted recent interest, and is heralded as a new frontier for materials discovery. We propose that the technique we use here for the growth of Mn_5O_8 can be applied to other metal precursors and oxidants to enable controlled growth of other metastable materials.

■ AUTHOR INFORMATION

Corresponding Author

*E-mail:Matthias.Young@colorado.edu (M.J.Y.).

Present Address

∥National Institute of Standards and Technology, Boulder, Colorado, 80305.

Notes

The authors declare no competing financial interest.

■ ACKNOWLEDGMENTS

■ REFERENCES

(1) Ovsyannikov, S. V.; Abakumov, A. M.; Tsirlin, A. A.; Schnelle, W.; Egoavil, R.; Verbeeck, J.; Van Tendeloo, G.; Glazyrin, K. V.; Hanfland, M.; Dubrovinsky, L. Perovskite-like Mn_2O_3: A Path to New Manganites. *Angew. Chem., Int. Ed.* **2013**, *52*, 1494–1498.

(2) Devaraj, S.; Munichandraiah, N. Effect of Crystallographic Structure of MnO_2 on Its Electrochemical Capacitance Properties. *J. Phys. Chem. C* **2008**, *112*, 4406–4417.

(3) Fritsch, S.; Navrotsky, A. Thermodynamic Properties of Manganese Oxides. *J. Am. Ceram. Soc.* **1996**, *79*, 1761–1768.

(4) Stobbe, E. R.; de Boer, B. A.; Geus, J. W. The Reduction and Oxidation Behaviour of Manganese Oxides. *Catal. Today* **1999**, *47*, 161–167.

(5) Fritsch, S.; Sarrias, J.; Rousset, A.; Kulkarni, G. U. Low-Temperature Oxidation of Mn_3O_4 Hausmannite. *Mater. Res. Bull.* **1998**, *33*, 1185–1194.

(6) Azzoni, C. B.; Mozzati, M. C.; Galinetto, P.; Paleari, A.; Massarotti, V.; Capsoni, D.; Bini, M. Thermal Stability and Structural Transition of Metastable Mn_5O_8: In Situ Micro-Raman Study. *Solid State Commun.* **1999**, *112*, 375–378.

(7) Bochu, B.; Deschizeaux, M. N.; Joubert, J. C.; Chenavas, J.; Collomb, a.; Levy, J. P.; Marezio, M.; Samaras, D.; Fillion, G. Structural Characterization, Preparation and Magnetic Properties of Several Room-Temperature Magnetic Oxides With the Perovskite-Like Structure. *Le J. Phys. Colloq.* **1977**, *38*, C1-C95–C1-C101.

(8) Singoredjo, L.; Korver, R.; Kapteijn, F.; Moulijn, J. Alumina Supported Manganese Oxides for the Low-Temperature Selective Catalytic Reduction of Nitric Oxide with Ammonia. *Appl. Catal., B* **1992**, *1*, 297–316.

(9) Tian, Z.-R.; Tong, W.; Wang, J.-Y.; Duan, N.-G.; Krishnan, V. V.; Suib, S. L. Manganese Oxide Mesoporous Structures: Mixed-Valent Semiconducting Catalysts. *Science* **1997**, *276*, 926–930.

(10) Jeong, D.; Jin, K.; Jerng, S. E.; Seo, H.; Kim, D.; Nahm, S. H.; Kim, S. H.; Nam, K. T. Mn_5O_8 Nanoparticles as Efficient Water Oxidation Catalysts at Neutral pH. *ACS Catal.* **2015**, *5*, 4624–4628.

(11) Thackeray, M. M.; David, W. I. F.; Bruce, P. G.; Goodenough, J. B. Lithium Insertion into Manganese Spinels. *Mater. Res. Bull.* **1983**, *18*, 461–472.

(12) Toupin, M.; Brousse, T.; Bélanger, D. Charge Storage Mechanism of MnO_2 Electrode Used in Aqueous Electrochemical Capacitor. *Chem. Mater.* **2004**, *16*, 3184–3190.

(13) Dagotto, E.; Hotta, T.; Moreo, A. Colossal Magnetoresistant Materials: The Key Role of Phase Separation. *Phys. Rep.* **2001**, *344*, 1–153.

(14) Moreo, a. Phase Separation Scenario for Manganese Oxides and Related Materials. *Science* **1999**, *283*, 2034–2040.

(15) Franchini, C.; Podloucky, R.; Paier, J.; Marsman, M.; Kresse, G. Ground-State Properties of Multivalent Manganese Oxides: Density Functional and Hybrid Density Functional Calculations. *Phys. Rev. B: Condens. Matter Mater. Phys.* **2007**, *75*, 1–11.

(16) Young, M. J.; Holder, A. M.; George, S. M.; Musgrave, C. B. Charge Storage in Cation Incorporated α-MnO2. *Chem. Mater.* **2015**, *27*, 1172–1180.

(17) Chigane, M.; Ishikawa, M. Manganese Oxide Thin Film Preparation by Potentiostatic Electrolyses and Electrochromism. *J. Electrochem. Soc.* **2000**, *147*, 2246–2251.

(18) Pang, S.-C.; Anderson, M. A.; Chapman, T. W. Novel Electrode Materials for Thin-Film Ultracapacitors: Comparison of Electrochemical Properties of Sol-Gel-Derived and Electrodeposited Manganese Dioxide. *J. Electrochem. Soc.* **2000**, *147*, 444–450.

(19) Neubeck, W.; Ranno, L.; Hunt, M. B.; Vettier, C.; Givord, D. Epitaxial MnO Thin Films Grown by Pulsed Laser Deposition. *Appl. Surf. Sci.* **1999**, *138–139*, 195–198.

(20) Nakamura, T.; Tai, R.; Nishimura, T.; Tachibana, K. Spectroscopic Study on Metallorganic Chemical Vapor Deposition of Manganese Oxide Films. *J. Electrochem. Soc.* **2005**, *152*, C584–C587.

(21) Rizzi, G. A.; Zanoni, R.; Di Siro, S.; Perriello, L.; Granozzi, G. Epitaxial Growth of MnO Nanoparticles on Pt(111) by Reactive Deposition of $Mn_2(CO)_{10}$. *Surf. Sci.* **2000**, *462*, 187–194.

(22) Burton, B. B.; Fabreguette, F. H.; George, S. M. Atomic Layer Deposition of MnO Using Bis(ethylcyclopentadienyl)manganese and H_2O. *Thin Solid Films* **2009**, *517*, 5658–5665.

(23) Nilsen, O.; Fjellvåg, H.; Kjekshus, A. Growth of Manganese Oxide Thin Films by Atomic Layer Deposition. *Thin Solid Films* **2003**, *444*, 44–51.

(24) Mattelaer, F.; Vereecken, P. M.; Dendooven, J.; Detavernier, C. Deposition of MnO Anode and MnO_2 Cathode Thin Films by Plasma Enhanced Atomic Layer Deposition Using the $Mn(thd)_3$ Precursor. *Chem. Mater.* **2015**, *27*, 3628–3635.

(25) George, S. M. Atomic Layer Deposition: An Overview. *Chem. Rev.* **2010**, *110*, 111–131.

(26) Lipson, A. L.; Puntambekar, K.; Comstock, D. J.; Meng, X.; Geier, M. L.; Elam, J. W.; Hersam, M. C. Nanoscale Investigation of Solid Electrolyte Interphase Inhibition on Li-Ion Battery MnO Electrodes via Atomic Layer Deposition of Al_2O_3. *Chem. Mater.* **2014**, *26*, 935–940.

(27) Pickrahn, K. L.; Park, S. W.; Gorlin, Y.; Lee, H.-B.-R.; Jaramillo, T. F.; Bent, S. F. Active MnO_x Electrocatalysts Prepared by Atomic Layer Deposition for Oxygen Evolution and Oxygen Reduction Reactions. *Adv. Energy Mater.* **2012**, *2*, 1269–1277.

(28) Simon, P.; Gogotsi, Y. Materials for Electrochemical Capacitors. *Nat. Mater.* **2008**, *7*, 845–854.

(29) Hall, P. J.; Mirzaeian, M.; Fletcher, S. I.; Sillars, F. B.; Rennie, A. J. R.; Shitta-Bey, G. O.; Wilson, G.; Cruden, A.; Carter, R. Energy Storage in Electrochemical Capacitors: Designing Functional Materials to Improve Performance. *Energy Environ. Sci.* **2010**, *3*, 1238–1251.

(30) Thackeray, M.; Division, C. T.; Program, E. T. Manganese Oxides for Lithium Batteries. *Prog. Solid State Chem.* **1997**, *25*, 3–4.

(31) Young, M. J.; Neuber, M.; Cavanagh, A. C.; Sun, H.; Musgrave, C. B.; George, S. M. Sodium Charge Storage in Thin Films of $MnO2$

Derived by Electrochemical Oxidation of MnO Atomic Layer Deposition Films. *J. Electrochem. Soc.* **2015**, *162*, A2753−A2761.

(32) Young, M. J.; Schnabel, H.-D.; Holder, A. M.; George, S. M.; Musgrave, C. B. Spinel LiMn2O4 Formed by Electrochemical Conversion of ALD-Grown MnO: Band-Diagram and Rate Analysis of Its Charge Storage Properties. *Adv. Funct. Mater.* **2016**. Under review.

(33) Miikkulainen, V.; Ruud, A.; Nilsen, O.; Laitinen, M.; Sajavaara, T.; Østreng, E.; Nilsen, O.; Laitinen, M.; Sajavaara, T.; Fjellvåg, H. Atomic Layer Deposition of Spinel Lithium Manganese Oxide by Film-Body-Controlled Lithium Incorporation for Thin-Film Lithium-Ion Batteries. *J. Phys. Chem. C* **2014**, *118*, 1258−1268.

(34) Ritala, M.; Puurunen, R. L.; Miikkulainen, V.; Leskelä, M.; Ritala, M.; Puurunen, R. L. Crystallinity of Inorganic Films Grown by Atomic Layer Deposition: Overview and General Trends. *J. Appl. Phys.* **2013**, *113*, 021301-1−021301-100.

(35) Knoops, H. C. M.; Elam, J. W.; Libera, J. a.; Kessels, W. M. M. Surface Loss in Ozone-Based Atomic Layer Deposition Processes. *Chem. Mater.* **2011**, *23*, 2381−2387.

(36) Hämäläinen, J.; Kemell, M.; Munnik, F.; Kreissig, U.; Ritala, M.; Leskelä, M. Atomic Layer Deposition of Iridium Oxide Thin Films from $Ir(acac)_3$ and Ozone. *Chem. Mater.* **2008**, *20*, 2903−2907.

(37) Elam, J.; Martinson, A.; Pellin, M.; Hupp, J. Atomic Layer Deposition of In2O3 Using Cyclopentadienyl Indium: A New Synthetic Route to Transparent Conducting Oxide Films. *Chem. Mater.* **2006**, *18*, 3571−3578.

(38) Seim, H.; Nieminen, M.; Niinistö, L.; Fjellvåg, H.; Johansson, L.-S. Growth of LaCoO3 Thin Films from β-Diketonate Precursors. *Appl. Surf. Sci.* **1997**, *112*, 243−250.

(39) Hämäläinen, J.; Munnik, F.; Ritala, M.; Leskelä, M. Study on Atomic Layer Deposition of Amorphous Rhodium Oxide Thin Films. *J. Electrochem. Soc.* **2009**, *156*, D418−D423.

(40) Hämäläinen, J.; Munnik, F.; Ritala, M.; Leskelä, M. Atomic Layer Deposition of Platinum Oxide and Metallic Platinum Thin Films from $Pt(acac)_2$ and Ozone. *Chem. Mater.* **2008**, *20*, 6840−6846.

(41) Martinson, A. B. F.; Devries, M. J.; Libera, J. A.; Christensen, S. T.; Hupp, J. T.; Pellin, M. J.; Elam, J. W. Atomic Layer Deposition of Fe_2O_3 Using Ferrocene and Ozone. *J. Phys. Chem. C* **2011**, *115*, 4333−4339.

(42) Nilsen, O.; Lie, M.; Foss, S.; Fjellvåg, H.; Kjekshus, A. Effect of Magnetic Field on the Growth of α-Fe_2O_3 Thin Films by Atomic Layer Deposition. *Appl. Surf. Sci.* **2004**, *227*, 40−47.

(43) Elam, J. W.; Groner, M. D.; George, S. M. Viscous Flow Reactor with Quartz Crystal Microbalance for Thin Film Growth by Atomic Layer Deposition. *Rev. Sci. Instrum.* **2002**, *73*, 2981−2987.

(44) Taylor, P. *Crystallographic Databases*; International Union of Crystallography: Chester, U.K., 1988; Vol. *44*.

(45) Izumi, F. Beyond the Ability of Rietveld Analysis: MEM-Based Pattern Fitting. *Solid State Ionics* **2004**, *172*, 1−6.

(46) Li, W.; Gibbs, G. V.; Oyama, S. T.; April, R. V. Mechanism of Ozone Decomposition on a Manganese Oxide Catalyst. 1. In Situ Raman Spectroscopy and Ab Initio Molecular Orbital Calculations. *J. Am. Chem. Soc.* **1998**, *120*, 9041−9046.

(47) Peterson, N. L.; Chen, W. K. Cation Self-Diffusion and the Isotope Effect in $Mn_{1-\delta}O$. *J. Phys. Chem. Solids* **1982**, *43*, 29−38.

(48) O'Keeffe, M. Diffusion in Oxides and Sulfides. In *Proceedings of the International Conference on Sintering and Related Phenomena*; Kuczynski, G. C., Hooton, N. A., Gibbon, C. F., Eds.; Springer: Notre Dame, IN, 1967; pp 57−96.

(49) Shannon, R. D.; Fischer, R. X. Empirical Electronic Polarizabilities in Oxides, Hydroxides, Oxyfluorides, and Oxychlorides. *Phys. Rev. B: Condens. Matter Mater. Phys.* **2006**, *73*, 1−28.

(50) Suntola, T. Atomic Layer Epitaxy. *Mater. Sci. Rep.* **1989**, *4*, 261−312.

(51) Ruetschi, P. Cation Vacancies in MnO2 and Their Influence on Electrochemical Reactivity. *J. Electrochem. Soc.* **1988**, *135*, 2663−2669.

(52) *CRC Handbook of Chemistry and Physics 2015−2016*, 96th ed.; Haynes, W. M., Lide, D. R., Bruno, T. J., Eds.; CRC Press/Taylor and Francis: Boca Raton, FL, 2015.

(53) Patterson, A. L. The Scherrer Formula for X-Ray Particle Size Determination. *Phys. Rev.* **1939**, *56*, 978−982.